Mechanical properties of milimetric silica aerogel particles produced through evaporative drying: A coupled experimental and discrete element approach

G. Hamelin, D. Jauffres, C. L. Martin, S. Meille, G. Foray

Mechanical properties of milimetric silica aerogel particles produced through evaporative drying: a coupled experimental and discrete element approach

G. Hamelin[a], D. Jauffrès[a], C. L. Martin[a], S. Meille[b], G. Foray[b]

[a] *Univ. Grenoble Alpes, CNRS, Grenoble INP, SIMaP, F-38000 Grenoble, France*
[b] *Univ Lyon, INSA-Lyon, Université Claude Bernard Lyon 1, CNRS UMR-5510, MATEIS, 7, Avenue Jean Capelle, 69621 Villeurbanne Cedex, France.*

Abstract

An alternative to supercritical drying to process silica aerogels is to apply evaporative drying to obtain particles that can then be used in the preparation of composite products. However, the mechanical behaviour of these particles is still poorly understood. In this work, millimetre-sized particles are studied combining experimental testing and discrete simulations. A statistical study of the compression of individual particle shows that the values of fracture strength are scattered because of the variability in shape, density and initial defects. The individual compression of aerogel particles inside an X-ray tomograph provides valuable information for understanding the influence of density on their elastic and fracture behaviors. Discrete simulations are calibrated using experimental data to reproduce numerically experimental compression observed inside the tomograph allowing the introduction of process induced particle defects. We show that these simulations can be used to determine the Young's modulus and fracture strength of aerogel particles.

Keywords: Silica aerogel, Particles, Uniaxial compression, Discrete Element Method, Fracture, X-ray tomography, Crack propagation

1. Introduction

In recent years, silica aerogels have attracted the interest of the thermal insulation industry. These materials indeed offer exceptional thermal performances with thermal conductivities as low as 12 $mW.m^{-1}.K^{-1}$, coupled with transparency, lightness and soundproofing properties, owing to their highly porous nanoscale pearl-necklace network of silica particles. The porosity level is generally over 90% with pores of approximately 10 nm [1]. These materials would be already largely used and produced were it not for their poor mechanical properties and high manufacturing cost, which makes their use very situational for now [2, 3, 4]. The evolution of regulations in the field of thermal insulation over the last years [5] seems to be a perfect context to promote new insulation materials offering enhanced properties for a reduced dedicated volume compared to conventional solutions in today's building, transportation and industry sectors.

Silica aerogels are produced by a sol-gel process followed by drying of the solvent used for the gel preparation [6, 7, 8]. The vast majority of studies dealing with silica aerogel mechanical properties concerns monolithic aerogels produced through supercritical drying, which is the privileged way to process high quality silica aerogel monoliths [9, 10, 11]. Very few studies focus

on aerogels produced through evaporative drying [12] and most of them deals with silica aerogel composites reinforced with a second phase during the gel formation [13, 14]. Evaporative drying, however, is a potential alternative for manufacturers looking for a lower production cost, as supercritical CO_2 is costly and creates additional constraints in the production process. One of the main drawbacks to aerogel production by evaporative drying is the occurrence of capillary forces as the liquid-vapor interface shape changes with time. These capillary forces cause serious problems for the production of large aerogel monoliths as they lead to the structure breakage, which results in particulate aerogels. Presently, the extremely high production cost of bulk silica aerogel panels strongly impedes their use in the building industry in this form. However, the use of aerogels in particle form is possible. Some of the typical insulation systems using aerogel particles are:

- window panels (raw aerogel particles sandwiched between two transparent panels) [15, 16]
- stiff composite panels (mixture of binder and aerogel particles) shaped in any geometry [17, 18]
- paintwork, construction sealants and plaster including aerogel particles [19, 20, 21]

In addition, it is possible to take advantage of aerogel particles obtained by evaporative drying for 3D printing of miniaturized insulators [22]. In all these insulation systems, micrometric and milimetric silica aerogel particles are used and the presence of over-nanometric porosity is not desirable (thermal conductivity of still air is greater than that of aerogel). The mechanical response of products such as stiff composite panels is mainly dependent on the mechanical behaviour of aerogel particles. A proper study of these properties would be very beneficial for the understanding of the failure mechanisms of the composite and the improvement of the current trade-off between strength, thermal performance and cost. Existing works on aerogel monoliths produced through supercritical drying have shown that the mechanical properties of silica aerogels are highly dependent on density [10, 9]. However, manufacturers can only partially rely on these studies to design composites, as it is suspected that evaporatively dried and supercritically dried silica aerogels exhibit structural properties that differ from one process to another. Indeed, high stresses induced during evaporative drying can generate defects such as cracks inside particles and density variations between particles. These are not (or to a lesser extent) observed in monolithic aerogels produced through supercritical drying.

To our best knowledge there is neither experimental nor numerical study available dealing with the mechanical behavior of aerogel particles produced through evaporative drying. The purpose of this work is thus to fill this knowledge gap through mechanical characterization of aerogel particles supplemented by modeling. In particular it is sought to understand and quantify the influence of pre-existing cracks and density variations on stiffness and strength. The millimetric size and irregular geometry of particles make it impossible to use conventional mechanical tests such as uniaxial compressions on cylindric samples, bending test on bars or brazilian tests. The characterization procedure chosen for this work is uniaxial compression of the aerogel particles themselves. This test is well adapted to the aerogel particles size and shape. More than fifty aerogel particles were compressed in this work, providing enough data for statistical analysis of particles strength. The mechanical tests were paired with density measurements and X-ray tomography in order to link the measured properties to the possible density variation and the presence of process induced cracks. The Discrete Element Method (DEM), particularly well-suited to simulate damage and crack propagation [23, 24, 25], has already been applied to silica

aerogels [26, 27]. Here, it is used to simulate particle compression and contribute to the analysis of experimental results.

The article is organized as follows. In section 2, the synthesis process and main properties of the studied silica aerogel are introduced. In section 3, experimental setups are presented. Section 4 presents the DEM model and the numerical procedures to generate aerogel particles made of discrete elements and simulate their compression. Results from both mechanical testing and DEM simulation are presented in section 5 and discussed in section 6.

2. Silica aerogel particles: synthesis and structure

2.1. Synthesis

Hydrophobic aerogels tested in this study were produced by Enersens company (Bourgoin-Jallieu, France) using an alkoxyde as a precursor for the sol-gel process: tetraethylorthosilicate (TEOS). The process uses ethanol as solvent. Once the gel is obtained an hydrophobic treatment adds trimethylsilyl groups on the free surface of the gel. This treatment partially counters the shrinkage of the gel during the following evaporative drying step [28, 29]. The aerogel hydrophobicity is also critical in its end use as a building material for durability reasons, as shown by [30]. Evaporative drying of the gel consists in increasing the temperature above the boiling point of ethanol. As a result of the evaporative drying and the capillary forces induced by the change of curvature of ethanol meniscus [31], the gel block densifies and breaks. The resulting aerogel has the shape of small translucent faceted particles of maximum size 5 mm (see Fig.1). The aerogel particles used for this study were sieved so that their dimension is between 1.00 and 1.25 mm. The final size range of the studied particles is typical of the largest particles used in stiff composite panels with bimodal particle size distribution [18].

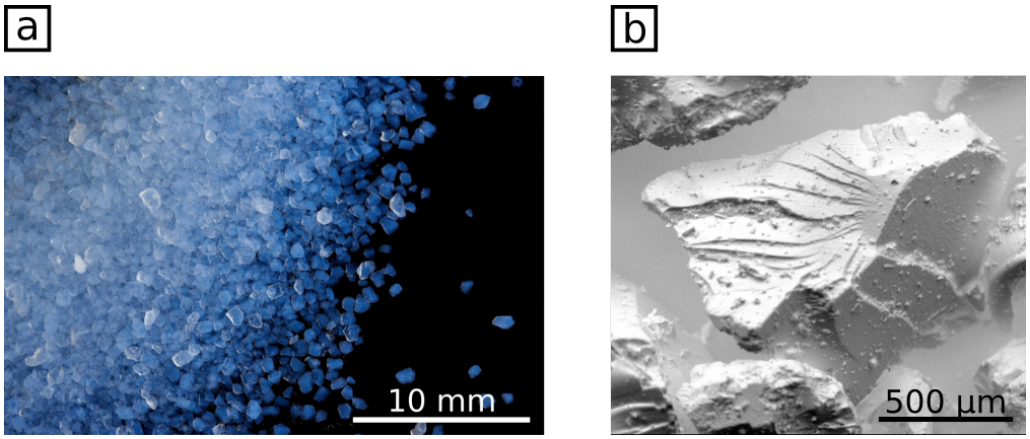

Figure 1: a) Silica aerogel particles produced by Enersens [32]. b) 1 mm silica aerogel particle observed with SEM, topographic contrast (no metallization). The aerogel particle is sprinkled with micrometric particles that are not an original feature of the 1 mm particles.

2.2. Structure and general precautions

The silica aerogel studied here has a nanoporous structure with a mean pore size of 10 nm [1]. The 4 nm silica primary particles are grouped in secondary patterns (agglomerates of primary

silica particles) of approximately 10 nm forming the three dimensional network responsible for the unique thermal and mechanical properties of the material. The porosity announced by the manufacturer is 90-98% [33]. All aerogel particles produced following the previous protocol have proven to be extremely brittle and can potentially break by simple friction while handling. For this reason, all aerogel particles for mechanical testing were handled by hand only with minimal transfer and immediately replaced in case of noticeable damage prior to testing. Tests were carried out at ambient temperature (20 to 23°C) and RH (40 to 60%).

3. Experimental setups

3.1. Density measurement

Density of aerogel particles is critical as it has been shown that elastic and fracture behaviours depend strongly on density [10, 9, 34, 35]. The density of the studied aerogel particles was measured using mercury picnometry on large particle batches (several hundreds of particles). Four particle batches were weighed and analyzed using a Micromeretics Autopore 4 with an increasing pressure from 0.001 to 0.206 MPa. The sample volume is measured at 0.036 MPa. Moreover, individual particle density was obtained by X-ray tomography volume measurements (see section 3.3).

3.2. Particle compression: statistical procedure

Two types of uniaxial compression tests have been carried out on aerogel particles. The first procedure is an experimental study of fracture inducing load under compression. More than 50 individual randomly selected particles were pressed up to failure. This procedure provides information on the scatter of the fracture force. The setup for these compression tests is shown in Fig.2a and was used at two different loading velocities (0.3 and 1.5 $\mathrm{mm.mn^{-1}}$) [9]. The load cell used had a nominal force of 22 N and a sensitivity of 0.01 N. The second procedure is presented hereafter.

3.3. Particle compression with X-ray tomography observation

Compression of individual aerogel particles within a X-ray tomograph was carried out. The compression device illustrated in Fig.2c was designed to be placed inside a X-ray tomograph (RX-Solution, Annecy, France). Particle compression is performed right after a first tomography scan at 40 kV, 250 μA. The density of each particle has been calculated before their compression from the volume determined from X-ray tomography and the mass measured using a XP26 Mettler Toledo microscale. Once a particle has been weighted, it only endures one transfer to the X-ray tomograph for initial scanning and is ready for mechanical testing with no additional manipulation. X-ray tomography is a convenient technique for monitoring aerogel fracture but some cautions are needed as these materials show a low absorption due to their extremely high porosity. Any material too dense compared to silica aerogels placed between the particle and the X-ray source or the CCD camera would absorb too many photons. It could induce a decreasing of the contrast of the scans or create artefacts. For this reason the window and the compression tools of the setup are made of polycarbonate. Low X-ray adsorption of polycarbonate and optimised thickness of material prevent artifacts. Particle compression was carried out at 1.2 $\mathrm{mm.mn^{-1}}$ and stopped at the first sign of fracture (detected by visual monitoring of 2D radiography). Due to some constraints of the setup, the force could not be recorded while the particle was compressed. The compression was paused several times (for a maximum of 20 seconds) once the particle had

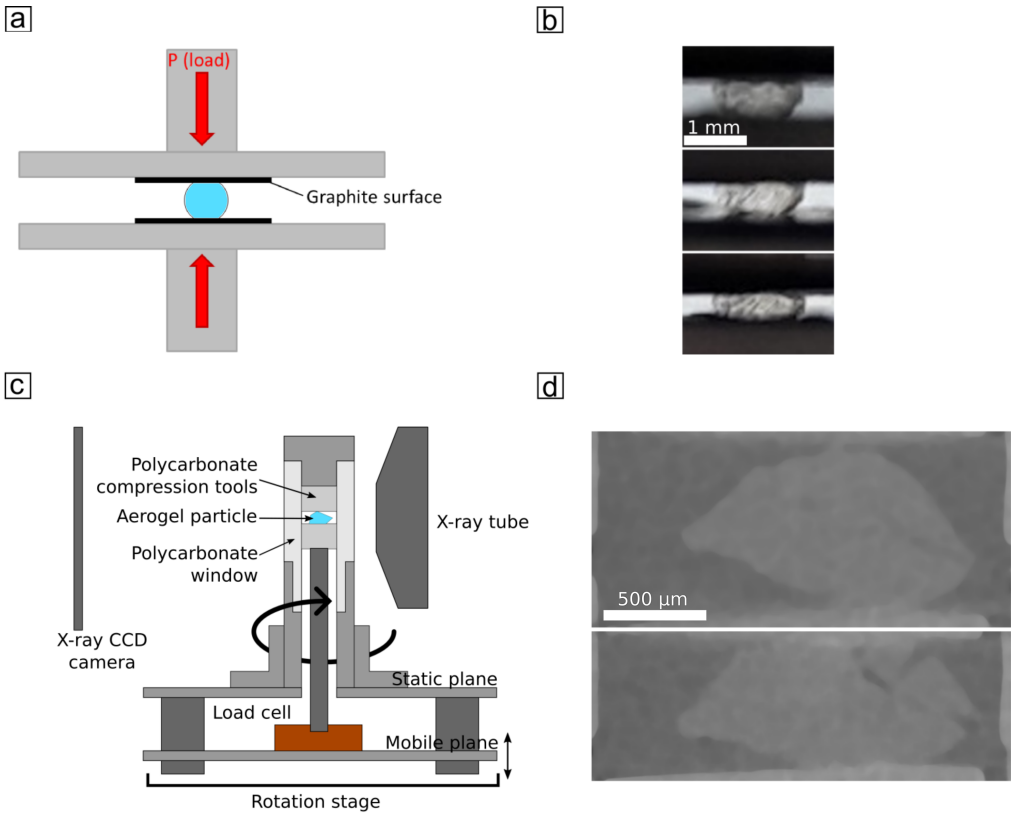

Figure 2: Compression setup for individual particle compression. a) Standard compression setup. b) Images of particles deformation while compressive load increase. c) Compression setup for X-ray tomograph compression. d) Tomographic cross section of a particle during fracture.

been compressed more than 30% of its initial height to record the force. This procedure eased the determination of the particle fracture force F_f by detecting with more accuracy the fracture of the particle. In that case, fracture force F_f and fracture height h_f were estimated as the mean value of two last recorded points with accordingly adjusted error bars. Fracture force and fracture height were determined for each particle. At least two scans were acquired with a voxel size of 2 μm, one just before the beginning of the compression and one once crack propagation has been detected in the aerogel particle. Particles were not unloaded for the final scan in order to maintain their integrity. Image processing of the tomography scans allowed the extraction of particles shape by applying a 3D median filter before segmentation of the aerogel phase by simple thresholding on graylevels (Fiji software [36]). Process induced cracks within particles were manually segmented as no automated method has given acceptable results for these features.

4. Discrete Element Method model

DEM is particularly well suited to study fracture and crack propagation of a large spectrum of materials. It was originally designed for the study of granular materials [37] but is also

adapted for continuous materials [23, 38, 39, 40, 24, 41]. Using DEM to study low-stiffness and brittle materials like silica aerogels was successfully carried out in several other studies [26, 27] with discrete elements representing primary silica particles, i.e. the silica particles forming the nanoscale pearl-necklace network of aerogels. Another simulation method, the hybrid finite-discrete element method (FDEM), is also well adapted to the study of continuous materials fracture as it combines the advantages of the finite element method for the study of continuum mechanical problems and the advantages of the discrete element method for the study of fracture phenomena [42, 43, 44]. FDEM has yet to be tested for aerogel particles fracture and this work will only focus on the use of DEM.

4.1. DEM framework

DEM simulations are performed with the in-house code dp3D using spherical discrete elements. Although silica aerogels are composed at the nanometer scale of discrete entities, their explicit representation within DEM would be computationally too demanding to model volumes as large as a few μm^3 [26]. DEM can nonetheless be used to model efficiently damage and fracture of a continuum media. Within this framework, the material is built as a random packing of spheres [41, 24]. Spheres do not represent real particles but are used to mesh a structure while providing a fully discontinuous framework handy for treating fractures. The interactions between spheres are predominantly defined by bonds that transmit normal and tangential forces and resisting moments. For bonds that have broken, if contact is restored, only normal forces in compression are transmitted. The forces acting on bonds have been described by Kumar et al. [41]. An equivalent radius at the bond between two spheres of radii R_p and R_q is defined as:

$$R^* = \frac{R_p R_q}{R_p + R_q} \tag{1}$$

The normal and tangential forces acting on the bond are given by simple linear elastic laws:

$$\mathbf{N} = -K_N \delta_N \mathbf{n} = -2\Sigma_N R^* \delta_N \mathbf{n} \tag{2}$$

$$\mathbf{T} = -K_T \delta_T \mathbf{t} = -2\Sigma_T R^* \delta_T \mathbf{t} \tag{3}$$

where δ_N and δ_T are the normal and tangential relative displacements between the two particle centers, K_N and K_T are local normal and tangential stiffnesses and $\mathbf{n}$ and $\mathbf{t}$ are the unit vectors normal and parallel to the contact plane, respectively. K_N and K_T vary with discrete elements dimension. It is thus preferred to use material parameters Σ_N and Σ_T with units of stress, which are independent of discrete element size.

We use the Rankine criterion for fracture, which is well adapted for brittle materials. The Rankine criterion states that a bond breaks when the maximum principal stress σ_R reaches the critical stress σ_Rc. In DEM, for a bond transmitting normal and tangential stress $\sigma_N = \frac{N}{4\pi R^{*2}}$ and $\sigma_T = \frac{T}{4\pi R^{*2}}$, σ_R is expressed as [23]:

$$\sigma_\mathrm{R} = \frac{1}{2}(\sigma_N + \sqrt{\sigma_N^2 + 4\sigma_T^2}) \tag{4}$$

4.2. Numerical preparation of aerogel particles

Aerogel particle volumes are extracted from X-ray tomography scans acquired just before compression as discussed in section 3. The X-ray tomography volumes are used to generate imprints of individual aerogel particles. These imprints take the form of 3D binarized images which are then used to cut the correct aerogel particle shape from a random packing of spherical discrete elements. This last step consists in removing all the discrete elements external to the imprint. The generation of the packing has been detailed in Kumar et al. [41]. In short, it consists of jamming a gas of discrete elements to a density of 0.5. This jammed packing is then further densified homothetically to a 0.65 relative density. Bonds are created by defining an interaction range of 1.075 meaning that spheres with centers less than 2×1.075 radius apart are bonded together. Kumar et al. used this protocol to describe how the Young's modulus and Poisson's ratio are related to the density of the numerical packing, average coordination and bond stiffness [41].

Here two different packings were used with respectively 25 μm and 15 μm radius discrete elements. These two sizes allow the fracture behaviour of the particles to be observed with two discretization refinements (smaller elements lead to a more refined discrete representation of the particle). Five aerogel particles have been generated following this protocol as illustrated in Fig.3. The process induced cracks observed inside the particles before compression can be introduced in the model by removing discrete elements located directly on the crack and by breaking the remaining bonds crossing the crack between the discrete elements which were not removed by the first step. Two numerical versions of each particle are thus generated, one crack-free and one with the observed initial cracks.

4.3. Calibration of numerical aerogel particle compression

The DEM simulated aerogel particles are compressed between two planes. Planes are considered as infinite radius particles and the discrete element-plane contact is a bond transmitting a purely normal force in compression as described by equation 2. The stiffness of the planes is chosen as identical to aerogel bond stiffness.

The DEM model parameters can be calibrated to reproduce the observed mechanical behaviour of particles. In order to calibrate normal and tangential stiffnesses of discrete elements, Σ_N and Σ_T, the data gathered during aerogel particle compression inside the X-ray tomograph are processed. For the same shape and the same orientation of the particles, the calibration is done individually for each aerogel particle by fitting the numerical load vs. displacement curves to the experimental fracture points (F_f,h_f) by tuning Σ_N. The shape of the numerical curves is very similar to the ones observed experimentally in uniaxial compression during statistical procedure (see Fig.4 and section 3.2). Kumar et al. [41] have shown that Σ_T/Σ_N is constant for a given Poisson's ratio. No practical solution has been found to measure the Poisson's ratio for the studied aerogels but literature suggests that silica aerogel Poisson's ratio exhibits no discernible variation with density or when using different synthesis processes. We assume that our aerogel Poisson's ratio is 0.2 for all particles analyzed in this work [45, 46]. The resulting Σ_T/Σ_N is 0.233 [41]. The fracture of the particle is calibrated by tuning the critical stress σ_{Rc} as defined by the Rankine criterion (eq.(4)). The calibration process is based on the DEM aerogel particles without any initial cracks.

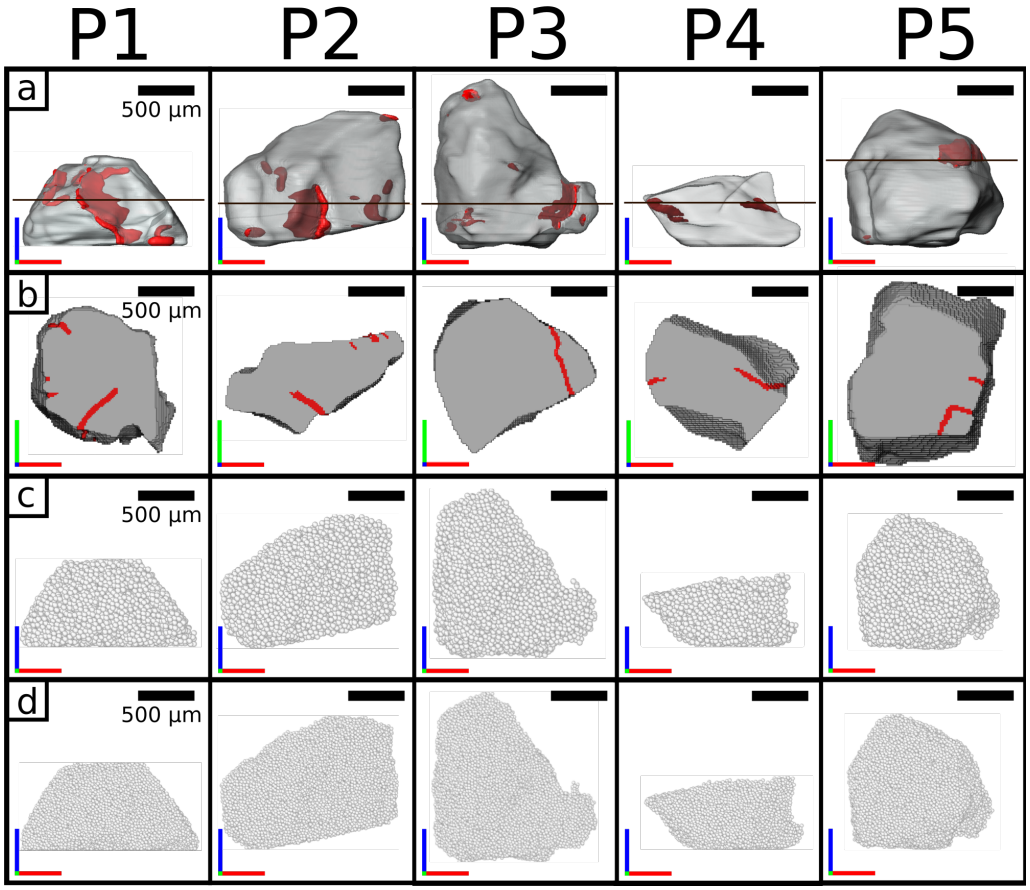

Figure 3: a) Aerogel particles with initial cracks reconstructed from X-ray tomography scans (in red). b) Cross section view within each particles at depth indicated on a). c) DEM aerogel particles prepared using 25 μm discrete elements. d) DEM aerogel particles prepared using 15 μm discrete elements. The numbering from P1 to P5 corresponds to a decreasing total crack length.

5. Results

5.1. Particle compression: statistical procedure

In total, 60 aerogel particles have been deformed at constant speed to initiate crack aperture from a critical defect. Ten measurements have been dismissed: eight because the fracture could not be accurately observed during the compression and two because of a non-satisfactory behaviour (brittle failure from particle directly to dust). Fracture is defined from the detection of a fall or stabilization of the force in the force/displacement curve together with a visual detection of the fracture of the compressed particle. Particle fracture is noticed by a vertical crack (parallel to the loading direction). A representative example of a force/displacement curve is illustrated in Fig.4. In most cases the force is still rising after fracture as the particle generally keeps its integrity, the different parts being held on by adhesive forces. Although somewhat arbitrary, this allows for a simple and consistent fracture criterion. The results obtained using this criterion are

summarized in Fig.5 (fracture force vs. normalized fracture height) for the two tested compression velocities. A large dispersion of the fracture force F_f and fracture height h_f is observed and no influence of compression velocity (in between 0.3 and 1.5 mm.mn^{-1}) is discernible. Particles compressed following this procedure have error bars of ±0.01 N for force and ±0.01 for strain. In an attempt to decorrelate the fracture force from particle size, the normalized force F_f/h_0^2 is calculated and plotted versus the initial height h_0 of the particles in Fig.6. Initial height is an approximate indicator of the particles size as the height/width ratio is close to unity for our aerogel particles. Normalizing force by the initial particle height to the square is a basic simplification of aerogel particle geometry to propose some measure of strength. It can not describe fully the complex geometry of particles. A similar simplification has been proposed in soil mechanics for sand particles with similar shapes [47].

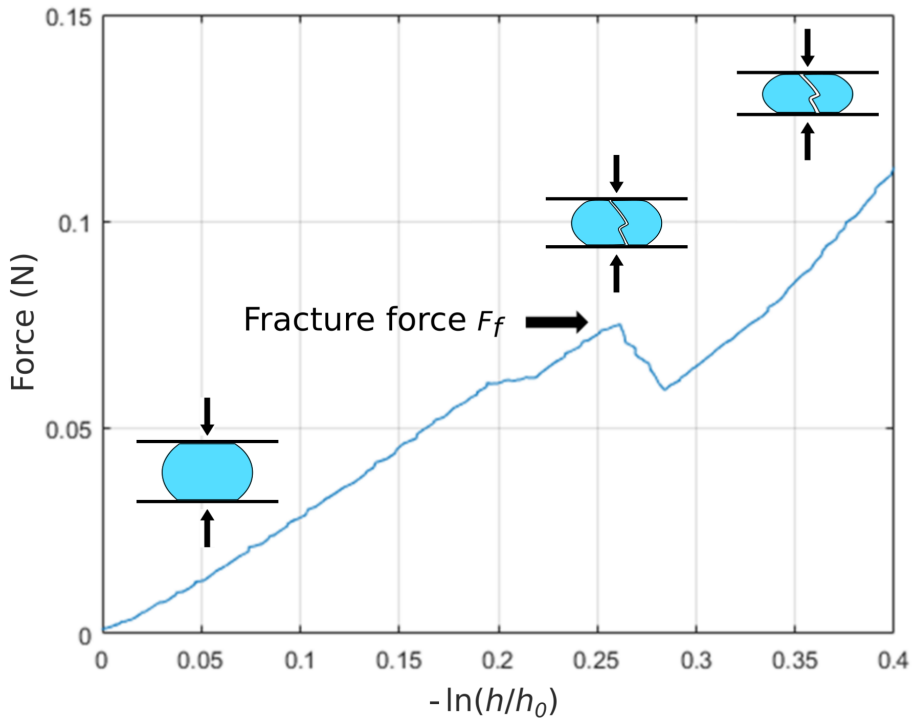

Figure 4: Experimental compression of an individual aerogel particle. h and h_0 are the current and initial sample heights, respectively.

5.2. Particle compression with X-ray tomography observation

Five aerogel particles have been compressed inside the X-ray tomograph tomograph giving information on particles shape, density and defects. Particles volume and density are presented in Table 1 as well as fracture force and normalized fracture height. Results from mercury picnometry carried on large batches of aerogel particles are also included in this table (MP). It is worth noting that particle P4, which is significantly smaller than others, departs from other particles

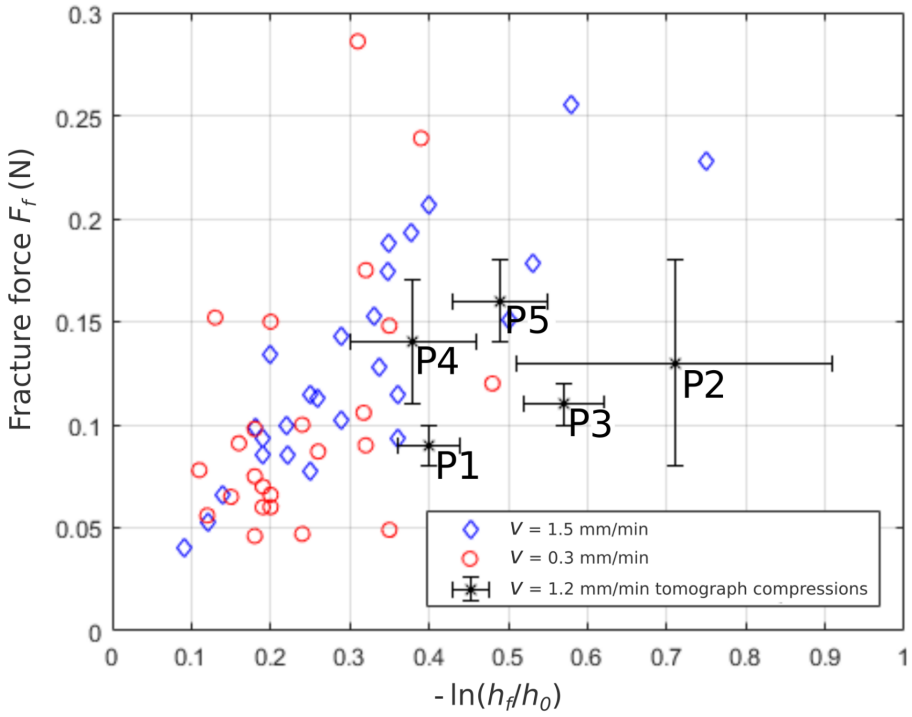

Figure 5: Fracture points (F_f,h_f) of aerogel particles following the two compression procedures : uniaxial particle compression carried out for two velocities. Samples P1 to P5 are those that have been scanned using X-ray tomography. Error bars of particles compressed following the statistical procedure are not shown for more clarity but are around 10% for fracture force and strain.

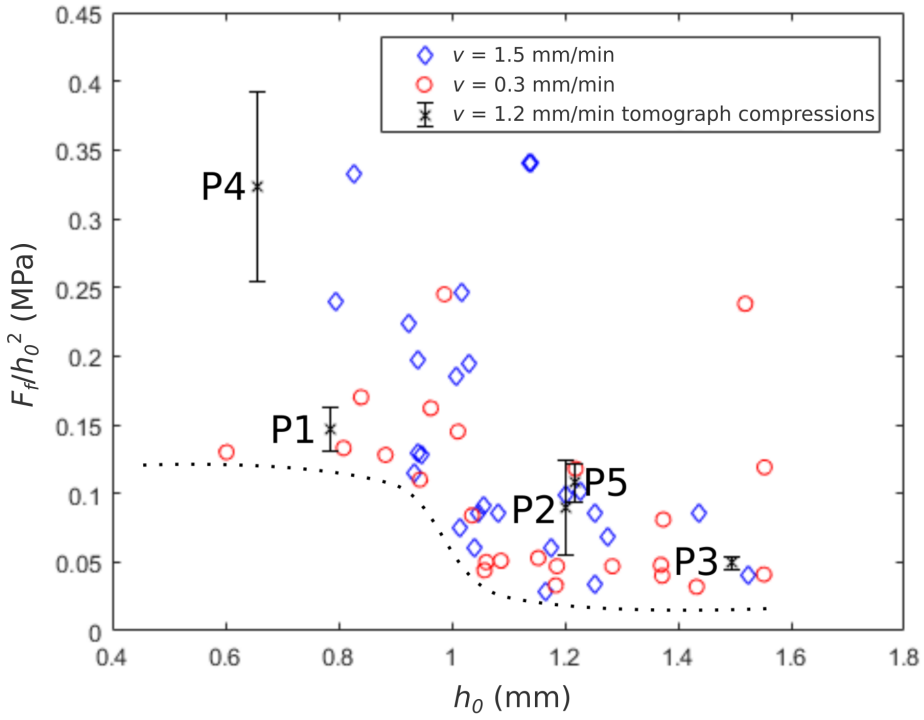

Figure 6: Normalized fracture force of compressed aerogel particles versus particle initial height h_0.

in terms of its density, which is significantly larger. At a first glance, density is not sufficient to warrant high fracture force, as P5 as a low density (0.10) and the highest load (0.16 N). The individually measured densities of P2, P3 and P5 are consistent with the mean density from mercury picnometry.

Table 1: Experimental results from tomograph particle compression and mercury picnometry (MP). h_f is particle height at fracture. Particle P1 was one of the first aerogel particles compressed inside the tomograph and density was not yet measured at this time.

	Density g/cm^3	Volume mm^3	-ln(h_f/h_0)	F_f N
P1	n.a.	0.722	0.40 ± 0.04	0.09 ± 0.01
P2	0.13 ± 0.02	0.684	0.71 ± 0.20	0.13 ± 0.05
P3	0.10 ± 0.02	1.076	0.57 ± 0.05	0.11 ± 0.01
P4	0.23 ± 0.04	0.300	0.38 ± 0.08	0.14 ± 0.03
P5	0.11 ± 0.02	0.981	0.49 ± 0.06	0.16 ± 0.02
MP	0.10 ± 0.01			

In Fig.5 the fracture forces of these five particles are illustrated together with the values from the statistical study and appear representative of the larger population tested outside the X-ray tomograph even if the values are slightly lower than the statistical study. This small difference might originate from the difference of friction with the compression tools between the two compression processes. Indeed, the graphite surface of the tools used during the statistical study induces less friction than the polycarbonate tools used for particles compressed inside the X-ray tomograph. Large error bars are due to the difficulty to detect the fracture under the tomograph setup (see section 3.3).

5.3. Calibration of DEM particles

The five particles scanned using X-ray tomography are used to recreate numerically compression tests using the DEM model described in section 4. The DEM model is calibrated as described in subsection 4.3 without introducing the initial cracks observed in X-ray tomography. For each particle the calibrated normal stiffness (Σ_N) and Rankine critical stress of the bonds between discrete elements (σ_{Rc}) are provided in Tables 2 and 3 for the two sizes of discrete elements used. These values are plotted in Fig.7 as a function of particle density. The differences noted are relatively limited on the calibrated parameters between the two different discretizations. Both Σ_N and σ_{Rc} increase with density, reflecting the stiffer and stronger mechanical response of denser particles.

Table 2: Calibration of bond normal stiffness Σ_N (Eq.(2))

	$\Sigma_N(R = 15\mu m)$ MPa	$\Sigma_N(R = 25\mu m)$ MPa	relative difference
P1	2.50	2.27	9.6%
P2	2.08	2.27	8.8%
P3	2.53	2.50	1.2%
P4	8.30	10.00	18.6%
P5	3.00	3.00	0%

Table 3: Calibration of critical bond strength σ_{Rc} (Eq.(4))

	$\sigma_{\mathrm{Rc}}(R = 15\mu m)$ MPa	$\sigma_{\mathrm{Rc}}(R = 25\mu m)$ MPa	relative difference
P1	0.15	0.11	30.8%
P2	0.24	0.23	4.3%
P3	0.20	0.20	0%
P4	0.40	0.32	22.2%
P5	0.25	0.21	17.4%

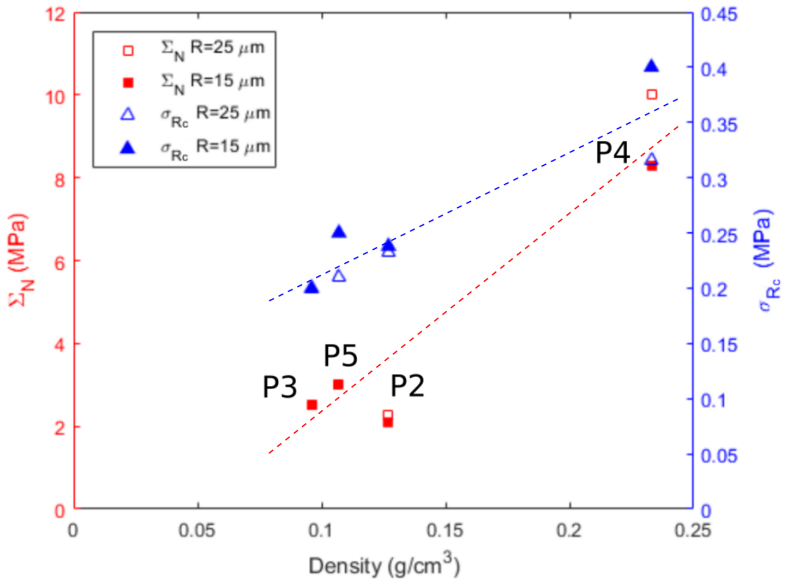

Figure 7: Calibrated DEM parameters Σ_N and σ_{Rc} for the five simulated aerogel particles as a function of particle density. Straight lines are drawn to guide the eye.

5.4. Crack propagation in DEM and influence of initial cracks

In the previous section the five DEM aerogel particles (P1-P5) scanned by X-ray tomography have been calibrated and tested without introducing the initial observed cracks (Fig.3a-b). By introducing these defects in the initial state of the particles before numerical compression, the fracture behaviour could be better described. Particle P1 has been chosen to illustrate the differences between DEM compression with and without initial cracks as illustrated in Fig.8. The initial and final cracks obtained during experimental compression (X-ray tomography) are showed in red on the volume reconstruction of the particle (Fig.8a) while broken bonds between discrete elements are showed on DEM particles (Fig.8b). The color of discrete elements indicates the chronological order of the fractured bonds from dark red to yellow. The cracks paths obtained in DEM aerogel particles do not follow the path observed with X-ray tomography.

The force versus displacement curves for the DEM particle P1 are shown in Fig.9. Fracture forces are measured on DEM curves by identifying the maximum on the force curve preceding the point corresponding to 0.1% broken bonds between discrete elements in the DEM particle. We can observe (Fig.9) a clear drop of the fracture force of DEM aerogel particles with the addition of initial cracks in the model. For the sake of completeness the experimental and numerical fracture behavior of the other four aerogel particles is provided in the Appendix. Fracture force values for the five DEM particles with and without initial cracks are summed up in Fig.10. These fracture forces are mean values as each aerogel particle version (with or without initial cracks, using either 25 μm or 15 μm discrete elements) was simulated with different discretizations. These five discretizations were simply obtained by providing five different seeds for the random generation of the very initial packings of discrete elements. The objective of these different packings is to estimate the scattering of the simulation results due to the discretization of aerogel particles. The resulting uncertainty of DEM fracture force due to the discretization depends slightly on the considered aerogel particle but remains below 7%.

6. Discussion

6.1. Macroscopic behaviour of aerogel particles in compression

As shown in Fig.5, fracture force values are quite scattered whatever the experimental procedure (outside or inside X-ray tomograph) as fracture depends on particle shape, size, orientation, density and initial defects. However, no clear difference was observed between the three tested velocities. Sensitivity to strain-rate for the tested aerogel particles can thus be considered negligible for compression rates between 0.3 and 1.5 mm.mn^{-1}. The five particles compressed inside the tomograph present fracture forces slightly lower than the results of the statistical study but still are coherent with the experimental dispersion. Error bars are large for some particles due to the difficulty to visually detect unambiguously the fracture while monitoring the X-ray projections of the particles during compression (see section 3.3). Particle P2 exhibits such a problem with thus large error bars.

The evolution of the normalized fracture force (units of a stress) with the initial height illustrated in Fig.6 enables to determine if the scatter in particle strength is mainly due to their size or to intrinsic properties (density and defects/cracks) and shape. No clear tendency in the normalized fracture load is observed with the variation of the particle initial height h_0. The normalized fracture force is still very dispersed, which suggests density variation, initial defects and shape have also a great influence on aerogel particle strength. Interestingly, normalized fracture forces are not observed below 0.1 MPa for small initial particle height h_0 (below 1mm). This

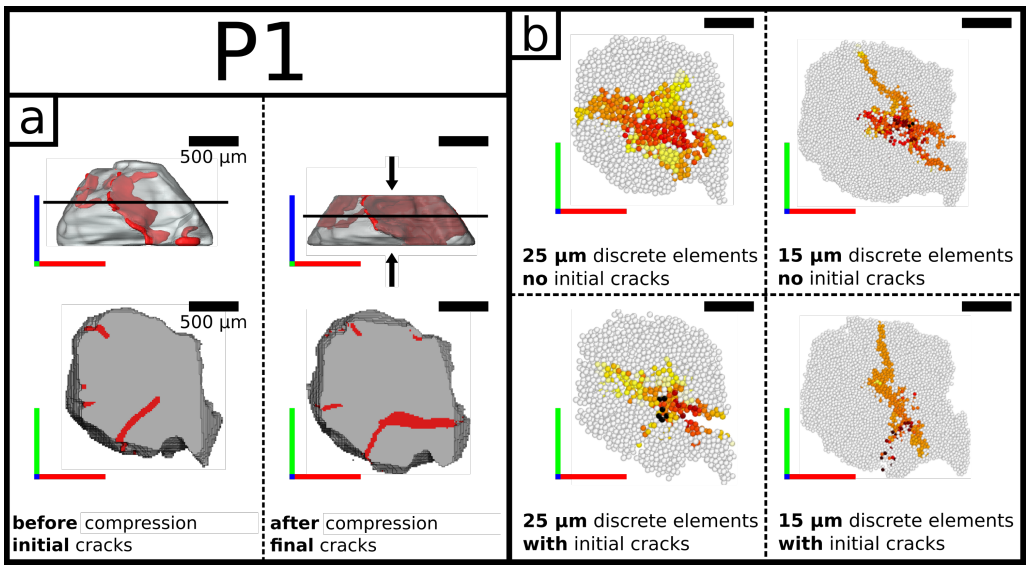

Figure 8: a) P1 particle volumes built from tomography compression test together with a cross section of interest. Top line: 3D representation, bottom line: cross section (location as indicated by a black line in top line) b) P1 particle cross sections at fracture load generated from coarse (25 μm) and fine (15 μm) discrete elements. Bond fractures are illustrated chronologically from dark red (earliest broken bonds) to yellow (latest broken bonds) and white (intact bonds).

could be explained by an increasing density and a lower probability to find critical initial defects for small particle volumes. Density measurements carried out on large particle populations with mercury picnometry and on individual particles for 4 out of 5 of the particles scanned with X-ray tomography tend to illustrate a possible link between size and density. Three particles scanned with X-ray tomography have a density close to the one measured over a large particle population with mercury picnometry $d_{MP} = 0.10 \pm 0.01$ g.cm^{-3} but the smallest particle studied (P4) is much denser ($d_{P4} = 0.23 \pm 0.04$ g.cm^{-3}). The three other particles having a density close to the mean density measured with mercury picnometry suggests the total volume occupied by particles as dense as P4 is small enough to have no significant impact on the mean density of a large population of particles.

6.2. Weibull distribution

The statistical dispersion of fracture load in compression for the large population of individual aerogel particles (52 compressions) has been fitted with a Weibull distribution function. The probability of particle fracture is plotted as a function of the normalized force $\sigma = \frac{F_f}{h_0^2}$ in Fig.11

The fracture probability P_f was fitted with the cumulative distribution function [48]:

$$P_f = 1 - \exp\left(-\left(\frac{\sigma - \sigma_u}{\sigma_0}\right)^m\right) \tag{5}$$

where σ_u, σ_0 and m are the translation, scale and shape fitted parameters, respectively. The Weibull parameter m gives some information on the dispersion of the normalized fracture force. m is low for materials with a large strength dispersion and high for materials with low dispersion.

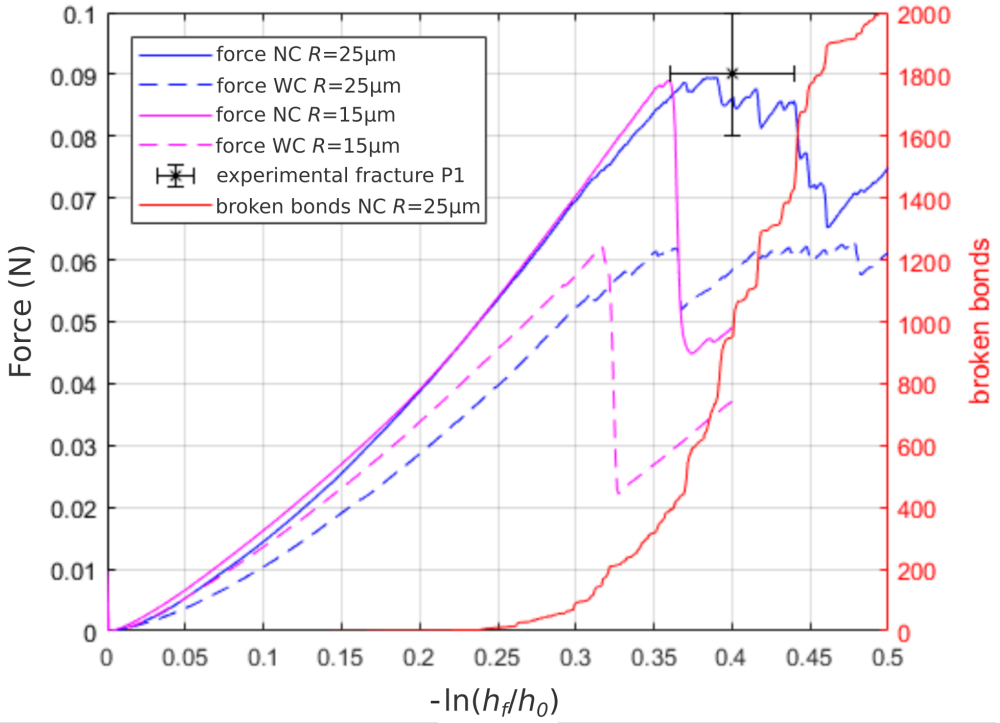

Figure 9: DEM compression of P1 with (WC) and without (NC) initial cracks generated from coarse (25 μm) and fine (15 μm) discrete elements. Experimental critical fracture of the particle is highlighted.

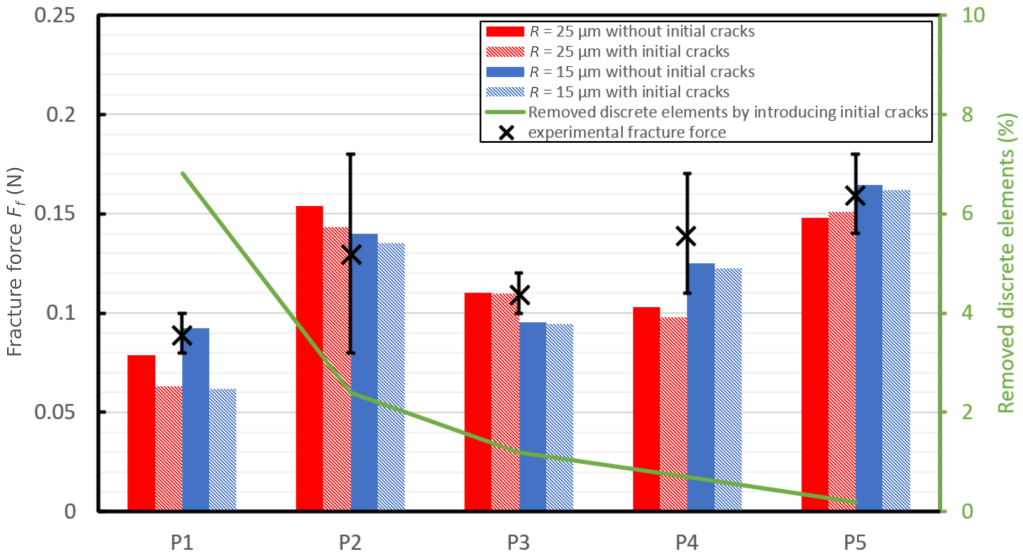

Figure 10: Fracture force for each simulated particle (P1-P5) with and without initial cracks introduced in the coarse (25 μm) and fine (15 μm) discrete elements mesh. The fraction of removed discrete element due to initial cracks introduction is plotted on the right hand side axis.

The parameter m also called Weibull modulus does not describe in our case a volume effect linked to the probability of presence of a critical defect size in a given volume. Silica aerogels are porous materials with a very high density of defects and do not fulfill the assumptions of Weibull analysis [49, 50]. Weibull distribution law is in our case only used as a fit of the cumulative probability distribution of our statistical study. The fit from Eq. (5) leads to σ_u = 29 kPa, σ_0 = 92 kPa and m = 1. The latter value is extremely low. As a reminder, the Weibull modulus of most ceramics, which are already considered as brittle materials with some defects, is generally between 5 and 10. Huillca et al. did a Weibull analysis on individual rock aggregates [51]. The rock aggregates are larger than our aerogel particles (5 to 40 mm) but have similar irregular shapes. They found a m parameter between 1.56 and 3.05 meaning our aerogel particles have a fracture behaviour more scattered than for brittle rocks with similar aggregate shape. This might be explained by large variations in density, in particle shape and the possible presence of initial defects. Weibull fits were also realized by Woignier et al. [46] on silica aerogel monoliths synthesized using supercritical drying. The modulus m is found between 4 and 7. It is difficult to compare these values with our results as Woignier et al. were not as much dependent on aerogel objects shape as we are with the present aerogel particles. The fact our value for m is much lower is yet not surprising as supercritical drying introduces much less defects and density scattering in the synthesised aerogel objects than evaporative drying.

6.3. DEM determination of Young's modulus and tensile strength

As indicated in Tables 2 and 3, the relative difference of calibration parameters Σ_N and σ_{Rc} between the two DEM discretization sizes is generally less than 20%. This low dependency to discretization means that the main factors influencing the calibration of the parameters Σ_N and σ_{Rc} are linked to the nature of the material and not to the numerical effects of the model itself.

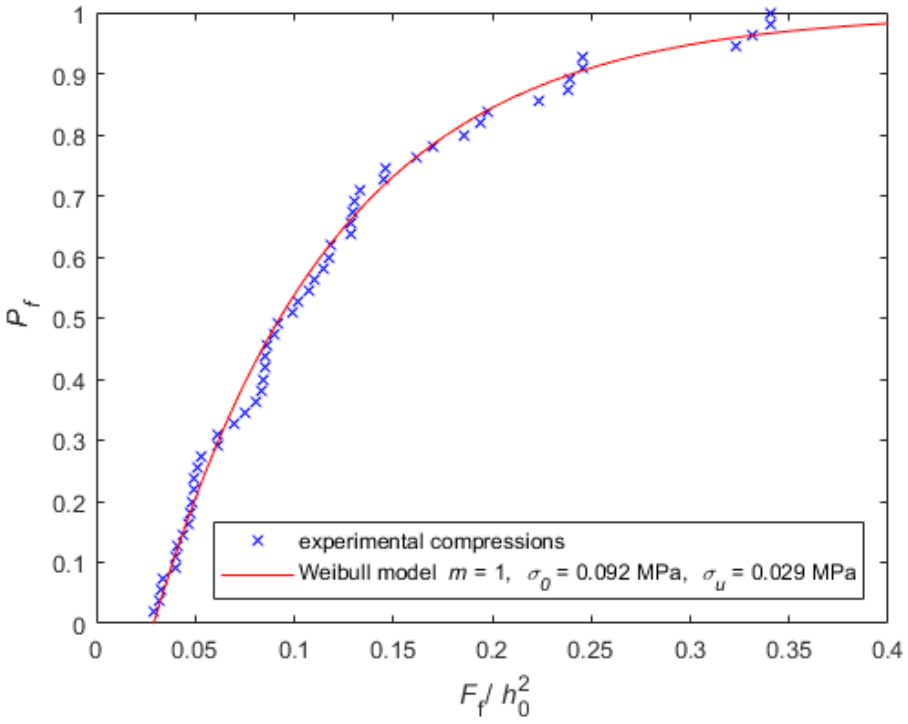

Figure 11: Weibull cumulative distribution fit carried out on the fracture by compression of aerogel particles. The fit leads to $m \approx 1$ in Eq.(5).

Σ_N and σ_{Rc} can thus be used with confidence to estimate the macroscopic Young's modulus and the fracture strength. The work of Kumar et al. [41] established relationships relating the discrete element bond stiffness to the macroscopic elastic behaviour of different packings obtained from various preparation routes including the one that was chosen in this work to model aerogel particles. These equations write:

$$E = Z_b D \Sigma_N \frac{\kappa^n}{2\pi} \frac{a_1 + a_2\alpha}{4 + a_3\alpha} \tag{6}$$

$$\alpha = \frac{1 - b_2\nu}{b_1 + b_3\nu} \tag{7}$$

where E Z_b, D and κ are the Young's modulus, the average coordination number, the packing density and the interaction range of the discrete element packing, respectively. The parameters n, a_i and b_i are fitted ($n = 2, a_1 = 0.42, a_2 = 7.45, a_3 = 8.68, b_1 = 0.55, b_2 = 3.02, b_3 = 5.75$) and originate from Kumar's work. The preparation route used here is defined as "weakly jammed" and results in a packing density of $D = 0.65$ and an average coordination number $Z_b = 6.56$ with an interaction range $\kappa = 1.075$.

Similarly to the Kumar et al. study, Radi et al. [23] established relationships between the macroscopic strength of a packing and the microscopic bond strength. Their equation writes:

$$\sigma_f = \sigma_{Rc}(c_1 Z_b D - c_2) \tag{8}$$

where σ_f is the macroscopic tensile strength, σ_{Rc} the Rankine critical stress of the bonds and c_i are fitted parameters ($c_1 = 0.124$, $c_2 = 0.067$).

These relations allow for the estimation of macroscopic properties from the calibrated microscopic parameters of the discrete element packing. For particles P2, P3 and P5 (of similar densities), the resulting estimations are $E = 0.7 \pm 0.1$ MPa and $\sigma_f = 100 \pm 10$ kPa. For particle P4 $E_{P4} = 2.6 \pm 0.3$ MPa and $\sigma_{fP4} = 165 \pm 26$ kPa. It is encouraging that our model and calibration method lead to a Young's modulus close to 1 MPa as this value is consistent with various studies on the elastic response of silica aerogels as function of their density [9, 10]. As expected, the dense particle P4 has a much higher Young's modulus than other particles. Concerning the estimated fracture strength, the previously cited literature [9, 10] also measured tensile strength (three point bending tests, brazilian tests) for various silica aerogels with various densities. For densities around 0.1 g.cm^{-3} the tensile strength ranges between 10 and 100 kPa. This is consistent with our value of 100 ± 10 kPa that is calculated from DEM simulations. According to Hiramatsu el al. [52], the fracture force normalized by the initial height to the square of the compressed particles is a correct estimation of the tensile strength. It is thus consistent to compare the fitted scale parameter σ_0 obtained with the Weibull fit performed previously in section 6.2 with the tensile strength obtained with Eq. (8). The two estimations of the tensile strength based on experimentation ($\sigma_0 = 92$ kPa) and simulation ($\sigma_f = 100 \pm 10$ kPa) agree very well. The use of DEM calibrated micro-parameters has the advantage of removing aerogel particle shape and orientation from the possible source of strength scattering. When considering aerogel particles with similar densities, the strength displays a coefficient of variation of 10% . This remaining scattering should originate mainly from the presence of initial cracks.

6.4. Influence of process induced cracks on the DEM mechanical behavior of aerogel particles

The introduction of cracks in DEM aerogel particles modifies their fracture behaviour. The objectives of the simulation are to quantify and to explain the influence of the initial cracks on

particles behaviour, as well as to check if the numerical crack propagation matches what was observed in tomography.

A positive point for the DEM model is that the final cracks observed for the four configurations as illustrated for particle P1 in (Fig.8) are located following a clearly identifiable path cutting the particles into two distinct main portions, especially for the thinly meshed particles (15 μm discrete elements) as the cracks are located in a much thinner zone compared to the 25 μm meshed particle. Particles with and without initial cracks do not fracture by following exactly the same path but the general behaviour is maintained. Still, the main cracks observed in DEM particles do not follow the fracture observed experimentally in tomography, except for the 25 μm discretized particle for which some similarities can be found. The DEM model fails to reproduce the final crack pattern once the fracture is initiated as it seems to depends too much on the discretization of the model. Also, we believe that the boundary conditions of the experiment at the onset of crack growth (interaction between the platens and the particle) are difficult to reproduce exactly. The complex crack growth patterns after fracture depend too much on the full strain history to be reproduced accurately in DEM.

However the initiation of the cracks is mostly correct with initial broken bonds (shown in black or dark red in Fig.8) localised around or at the extremity of the initial cracks. After its initiation, the crack follows a path imposed by the discrete element packing and so does not describe the real case. Thinly discretized particles (15 μm) are best suited for the acquisition of precise crack patterns but are four to five times more computationally expensive compared to the 25 μm discretized particles.

Although the cracks morphological differences are minor for particle P1 with and without initial cracks, there is a quantitative difference between particles with and without initial cracks with a drop of the fracture force in compression of approximately 30% (Fig.9). Fig.10 indicates that particle P1 is the only simulated particle exhibiting a fracture force drop superior to 15% after initial cracks are introduced in the model. This is consistent with the fact that particle P1 is the particle with the largest relative number of discrete elements removed in the crack modelling process (7% versus 2.5% for P2, the second most impacted particle). Particles P2 to P5 exhibit much smaller variations of the fracture force when initial cracks are introduced. In general, a decrease of the fracture force is almost always observed when initial cracks are introduced but, apart from particle P1, it is low. It is thus safe to conclude that the initial cracks introduced in the DEM aerogel particles following our procedure have rarely a large influence both on the cracks morphology after crack initiation and on the fracture force values. It might be due to the orientation and localisation of the initial crack patterns which rarely weaken the aerogel particles in the uniaxial compression direction. The probability to find a well located and oriented crack increases with the amount of initial damage and only P1 presents a crack parallel to the loading conditions and located in a zone experiencing a high tensile stress (typically close to the center of the particle). It could also explain why tensile strengths lower than 0.1 MPa were not observed for small particles during experimental uniaxial compression (see Fig.6) as the probability to find a well located and oriented defect might increase with particle volume.

7. Conclusions

Experimental compression tests and DEM simulations were carried out in order to investigate the mechanical behavior of millimetric silica aerogel particles produced by evaporative drying.

A first experimental statistical study has shown that the values of fracture force are very much scattered, as quantified by Weibull statistics. This is due to the combination of the vari-

ability of the particles shape, orientation, density and the presence of initial defects. In order to decorrelate the influence of these parameters, an original methodology based on individual X-ray tomography images of particles coupled with DEM simulations is proposed. Individual density assessment of aerogel particles based on X-ray tomography volumes has shown significant density variation (0.1 to 0.23 g/cm^3) that explains an important part of the scattering. Particles with similar densities still exhibit important normalized fracture force variations that can be attributed to particles shape and orientation and to the potential presence of initial defects in the particles during compression test. The methodology consists of the numerical replication with DEM of a compression experiment, using the particle morphology and orientation from X-ray tomography images. The calibrated DEM parameters are used to assess the material Young's modulus and strength. This methodology gives encouraging results, with Young's modulus (0.7 ± 0.1 MPa) and strength (100 ± 10 kPa) values for a density of around 0.1 g/cm^3 all consistent with literature data on supercritically dryed monolithic aerogels. The remaining small scattering in strength (coefficient of variation of 10%) is attributed to the methodology uncertainty itself and the inherent variability due to the presence of initial defects. The relatively modest influence of process induced defects is confirmed by DEM modeling that shows that for particle in compression, the initial cracks within the sample have rarely a highly detrimental effect on strength. It is consistent with the fact that the obtained value for strength is similar to reported values for monolithic aerogel of similar density. Still, one should keep in mind that for a purely homogeneous tensile loading (which might happen within a composite) the presence of initial cracks in the aerogel particle will probably be more critical.

8. Acknowledgements

The authors are grateful to Pierre Lhuissier, Xavier Bataillon and Cyril Rajon (SIMaP laboratory, St Martin d'Hères, France) for the help provided designing the uniaxial compression device used during X-ray tomography. The french region Auvergne Rhône-Alpes (COMPASS project) is greatly acknowledged for its financial support. The companies ENERSENS (Bourgoin-Jallieu, France) and EDF (Paris, France) are also acknowledged for their involvement in this work.

Appendix A. Fracture of DEM aerogel particles P2 to P5

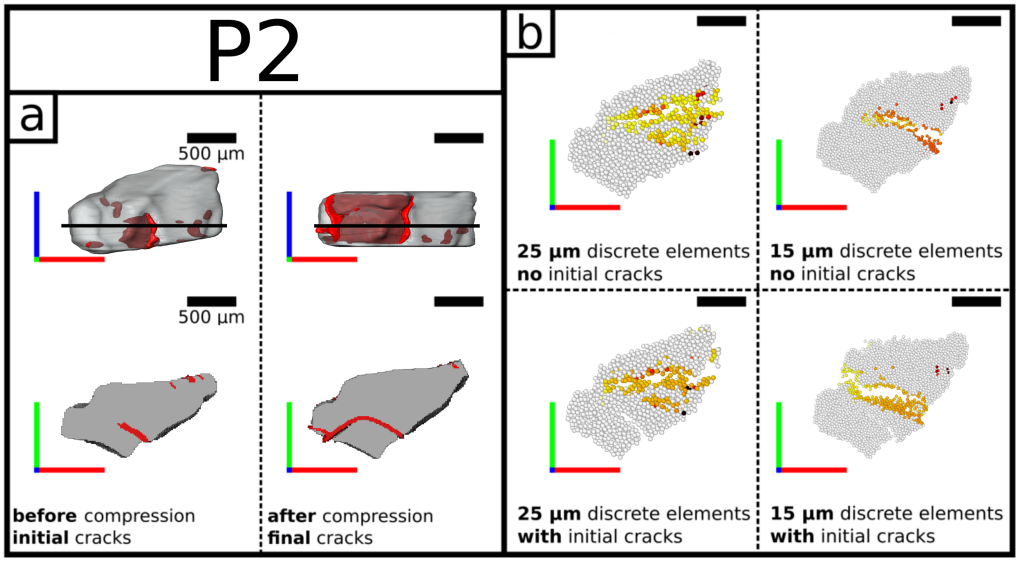

Figure A.12: a) P2 particle volumes built from tomography compression test. b) P2 particle volumes built using 2 types of discrete elements with DEM. The bond fractures are illustrated chronologically from hot to cold colors.

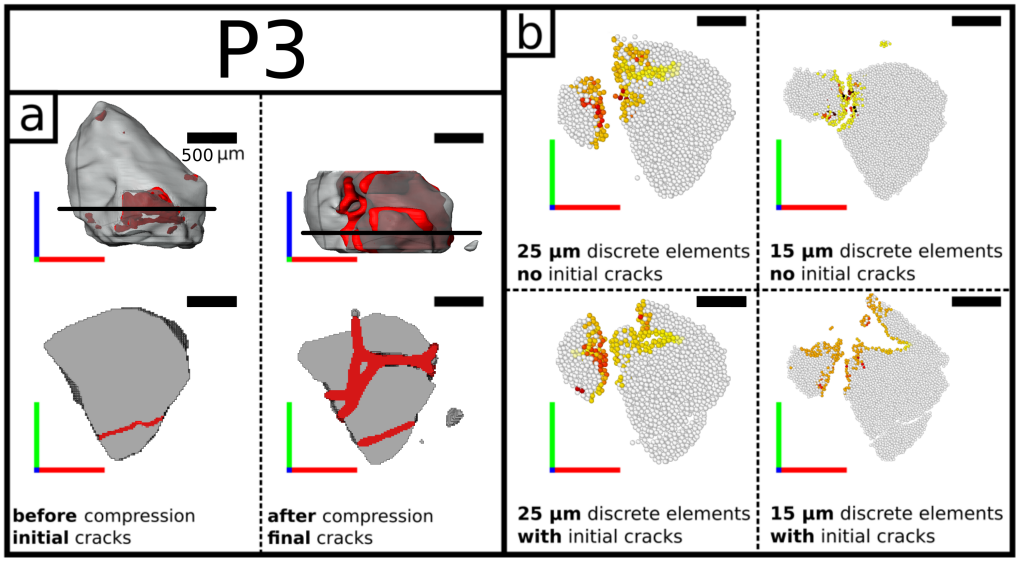

Figure A.13: a) P3 particle volumes built from tomography compression test. b) P3 particle volumes built using 2 types of discrete elements with DEM. The bond fractures are illustrated chronologically from hot to cold colors.

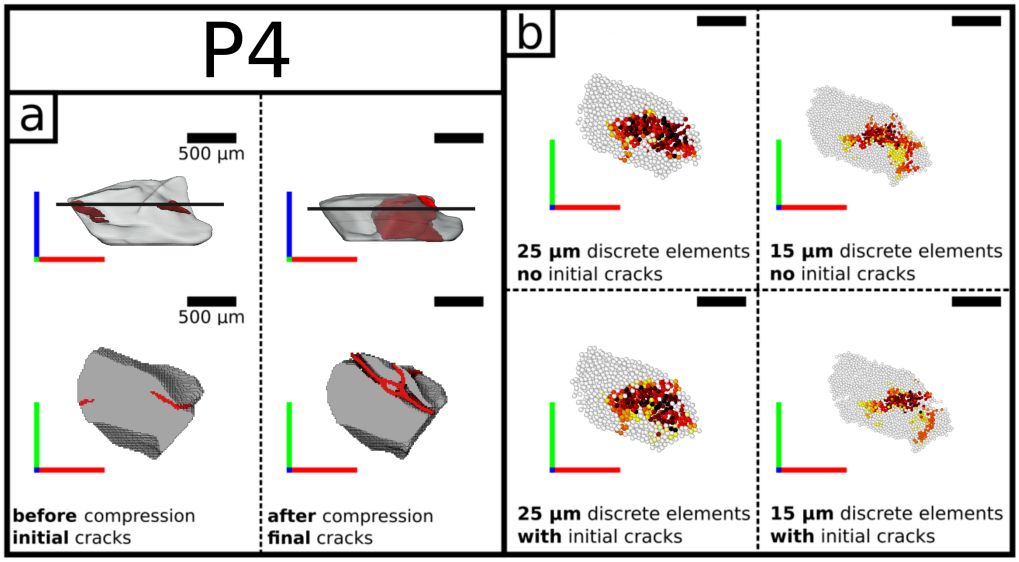

Figure A.14: a) P4 particle volumes built from tomography compression test. b) P4 particle volumes built using 2 types of discrete elements with DEM. The bond fractures are illustrated chronologically from hot to cold colors.

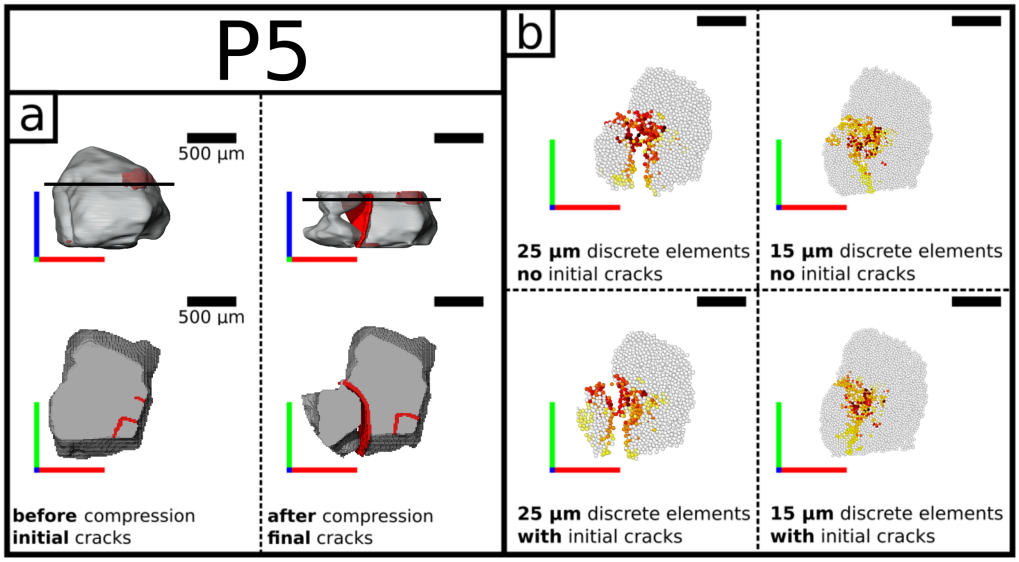

Figure A.15: a) P5 particle volumes built from tomography compression test. b) P5 particle volumes built using 2 types of discrete elements with DEM. The bond fractures are illustrated chronologically from hot to cold colors.

463

464

References

[1] L. Roiban, G. Foray, Q. Rong, A. Perret, D. Ihiawakrim, K. Masenelli-Varlot, E. Maire, B. Yrieix, Advanced three dimensional characterization of silica-based ultraporous materials, RSC Advances 6 (2016) 10625–10632.

[2] Kalwall products, https://www.kalwall.com/kalwall-products/, ???? Accessed: 2020-06-06.

[3] Yale university sculpture building in new haven connecticut usa, https://www.cabotcorp.com/solutions/applications/construction/daylighting/yale-university-sculpture-building-in-new-haven-connecticut-usa, ???? Accessed: 2020-06-06.

[4] M. Ganobjak, S. Brunner, J. Wernery, Aerogel materials for heritage buildings: Materials, properties and case studies, Journal of Cultural Heritage 42 (2020) 81–98.

[5] All you need to know about the 2020 thermal regulation, https://hirschisolation.fr/en/constuire_renover/tout-savoir-sur-la-reglementation-thermique-2020/, ???? Accessed: 2020-06-06.

[6] M. Aegerter, N. Leventis, M. Koebel, Aerogels handbook (Advances in Sol-Gel Derived Materials and Technologies), pp. 21–123.

[7] J. M. Schultz, K. I. Jensen, F. H. Kristiansen, Super insulating aerogel glazing, Solar Energy Materials and Solar Cells 89 (2005) 275–285.

[8] T. Błaszczyński, A. Ślosarczyk, M. Morawski, Synthesis of silica aerogel by supercritical drying method, Procedia Engineering 57 (2013) 200–206.

[9] J. C. Wong, H. Kaymak, S. Brunner, M. M. Koebel, Mechanical properties of monolithic silica aerogels made from polyethoxydisiloxanes, Microporous and Mesoporous Materials 183 (2014) 23–29.

[10] T. Woignier, J. Primera, A. Alaoui, P. Etienne, F. Despestis, S. Calas-Etienne, Mechanical Properties and Brittle Behavior of Silica Aerogels, Gels 1 (2015) 256–275.

[11] K. E. Parmenter, F. Milstein, Mechanical properties of silica aerogels, Journal of Non-Crystalline Solids (1998).

[12] S. Hæreid, M. A. Einarsrud, G. W. Scherer, Mechanical strengthening of TMOS-based alcogels by aging in silane solutions, Journal of Sol-Gel Science and Technology 3 (1994) 199–204.

[13] H. Sai, R. Fu, J. Xiang, Y. Guan, F. Zhang, Fabrication of elastic silica-bacterial cellulose composite aerogels with nanoscale interpenetrating network by ultrafast evaporative drying, Composites Science and Technology 155 (2018) 72–80.

[14] S. Yun, H. Luo, Y. Gao, Ambient-pressure drying synthesis of large resorcinol-formaldehyde- reinforced silica aerogels with enhanced mechanical strength and superhydrophobicity, Journal of Materials Chemistry A 2 (2014) 14542–14549.

[15] K. Chen, A. Neugebauer, T. Goutierre, A. Tang, L. Glicksman, L. J. Gibson, Mechanical and thermal performance of aerogel-filled sandwich panels for building insulation, Energy and Buildings 76 (2014) 336–346.

[16] S. C. Joshi, A. A. Sheikh, A. Dineshkumar, Z. Yong, Development and evaluation of aerogel-filled BMI sandwich panels for thermal barrier applications, AIMS Materials Science 3 (2016) 938–953.

[17] A. Int, S. Sa, R. La, S. B. Bk, Fiche technique - Sto-Aevero Panneau isolant intérieur, Technical Report 58 cm, 2019.

[18] B. Yrieix, B. Morel, G. Foray, A. Bogner, Aerogel based material that is superinsulating at atmospheric pressure, 2012. Patent WO/2012/168617.

[19] R. Aksu, B. SAygı, Investigation of silica aerogels effect on paint characteristics (2019) 139–146.

[20] M. Ganobjak, E. Kralova, Impact Verification of Aerogel Insulation Paint on Historic Brick Facades, IOP Conference Series: Materials Science and Engineering 245 (2017).

[21] S. Fantucci, E. Fenoglio, G. Grosso, V. Serra, V. Marino, M. Dutto, Development of an aerogel-based thermal coating for the energy retrofit and the prevention of condensation risk in existing buildings, Science and Technology for the Built Environment 25 (2019) 1178–1186.

[22] S. Zhao, G. Siqueira, S. Drdova, D. Norris, C. Ubert, A. Bonnin, S. Galmarini, M. Ganobjak, Z. Pan, S. Brunner, G. Nyström, J. Wang, M. M. Koebel, W. J. Malfait, Additive manufacturing of silica aerogels, Nature 584 (2020) 387–392.

[23] K. Radi, D. Jauffrès, S. Deville, C. L. Martin, Elasticity and fracture of brick and mortar materials using discrete element simulations, Journal of the Mechanics and Physics of Solids 126 (2019) 101–116.

[24] D. André, J. Girardot, C. Hubert, A novel DEM approach for modeling brittle elastic media based on distinct lattice spring model, Computer Methods in Applied Mechanics and Engineering 350 (2019) 100–122.

[25] D. O. Potyondy, P. A. Cundall, A bonded-particle model for rock 41 (2004) 1329–1364.

[26] Q. Liu, Z. Lu, M. Zhu, Z. Yuan, Z. Yang, Z. Hu, J. Li, Simulation of the tensile properties of silica aerogels: The effects of cluster structure and primary particle size, Soft Matter 10 (2014) 6266–6277.

[27] E. Guesnet, B. Bénane, D. Jauffrès, C. L. Martin, G. P. Baeza, G. Foray, S. Meille, C. Olagnon, B. Yrieix, Why fumed and precipitated silica have different mechanical behavior: Contribution of discrete element simulations, Journal of Non-Crystalline Solids 524 (2019) 119646.

[28] A. P. Rao, A. V. Rao, G. M. Pajonk, Hydrophobic and physical properties of the two step processed ambient pressure dried silica aerogels with various exchanging solvents, Journal of Sol-Gel Science and Technology 36 (2005) 285–292.
[29] V. D. Land, T. M. Harris, D. C. Teeters, Processing of low-density silica gel by critical point drying or ambient pressure drying, Journal of Non-Crystalline Solids 283 (2001) 11–17.
[30] B. Chal, B. Yrieix, L. Roiban, K. Masenelli-Varlot, J. M. Chenal, G. Foray, Nanostructured silica used in super-insulation materials (SIM), hygrothermal ageing followed by sorption characterizations, Energy and Buildings 183 (2019) 626–638.
[31] T. Woignier, J. Phalippou, F. Despetis, S. C.-e. Aerogel, P. Lisa, Aerogel Processing, 2018.
[32] Enersens, kwark granule, `http://enersens.fr/fr/kwark-granules/`, ???? Accessed: 2020-08-09.
[33] ENERSENS, Kwark granule - fiche technique, Technical Report, 2015.
[34] S. O. Kucheyev, M. Stadermann, S. J. Shin, J. H. Satcher, S. A. Gammon, S. A. Letts, T. Van Buuren, A. V. Hamza, Super-compressibility of ultralow-density nanoporous silica, Advanced Materials 24 (2012) 776–780.
[35] A. Faivre, L. Duffours, P. Colombel, F. Despetis, Mechanical behaviour of aerogels and composite aerogels submitted to specific penetration tests, Journal of Sol-Gel Science and Technology (2018) 1–9.
[36] Fiji - imagej, `https://imagej.net/Fiji`, ???? Accessed: 2020-15-12.
[37] P. A. Cundall, O. D. L. Strack, A discrete numerical model for granular assemblies, Géotechnique 29 (1979) 47–65.
[38] D. André, M. Jebahi, I. Iordanoff, J. luc Charles, J. Ô. Néauport, Using the discrete element method to simulate brittle fracture in the indentation of a silica glass with a blunt indenter, Computer Methods in Applied Mechanics and Engineering 265 (2013) 136–147.
[39] B. D. Le, F. Dau, J. L. Charles, I. Iordanoff, Modeling damages and cracks growth in composite with a 3D discrete element method, Composites Part B: Engineering 91 (2016) 615–630.
[40] W. Leclerc, H. Haddad, M. Guessasma, On the suitability of a Discrete Element Method to simulate cracks initiation and propagation in heterogeneous media, International Journal of Solids and Structures 108 (2017) 98–114.
[41] R. Kumar, S. Rommel, D. Jauffrès, P. Lhuissier, C. L. Martin, Effect of packing characteristics on the discrete element simulation of elasticity and buckling, International Journal of Mechanical Sciences 110 (2016) 14–21.
[42] B. S. A. Tatone, G. Grasselli, International Journal of Rock Mechanics & Mining Sciences A calibration procedure for two-dimensional laboratory-scale hybrid fi nite – discrete element simulations, International Journal of Rock Mechanics and Mining Sciences 75 (2015) 56–72.
[43] M. Hazay, Introduction to the Combined Finite- Discrete Element Method (2004) 30–32.
[44] C. Yan, Y. Zheng, D. Huang, G. Wang, A coupled contact heat transfer and thermal cracking model for discontinuous and granular media, Computer Methods in Applied Mechanics and Engineering 375 (2021) 113587.
[45] D. Haranath, P. B. Wagh, G. M. Pajonk, A. Venkateswara Rao, Influence of sol-gel processing parameters on the ultrasonic sound velocities in silica aerogels, Materials Research Bulletin 32 (1997) 1079–1089.
[46] T. Woignier, J. Primera, A. Alaoui, F. Despetis, S. Calas-Etienne, A. Faivre, L. Duffours, C. Levelut, P. Etienne, Techniques for characterizing the mechanical properties of aerogels, volume 93, 2020.
[47] G. R. McDowell, M. D. Bolton, On the micromechanics of crushable aggregates, Geotechnique 48 (1998) 667–679.
[48] W. Weibull, A statistical theory of the strength of materials, Generalstabens Litografiska Anstalts Fo rla (1939).
[49] C. Lu, R. Danzer, F. D. Fischer, Scaling of fracture strength in ZnO: Effects of pore/grain-size interaction and porosity, Journal of the European Ceramic Society 24 (2004) 3643–3651.
[50] F. W. Zok, On weakest link theory and Weibull statistics, Journal of the American Ceramic Society 100 (2017) 1265–1268.
[51] Y. Huillca, M. Silva, C. Ovalle, J. C. Quezada, S. Carrasco, G. E. Villavicencio, Modelling size effect on rock aggregates strength using a DEM bonded-cell model, Acta Geotechnica 0123456789 (2020).
[52] Y. Hiramatsu, Y. Oka, Determination of the tensile strength of rock by a compression test of an irregular test piece, International Journal of Rock Mechanics and Mining Sciences and 3 (1966) 89–90.